J. Fluid Mech. (1984), *vol.* 140, *pp.* 343–353
Printed in Great Britain

Flow in a small annulus between concentric cylinders

By M. LÜCKE†, M. MIHELCIC, K. WINGERATH
Institut für Festkörperforschung der Kernforschungsanlage Jülich, D-5170 Jülich, West Germany
AND G. PFISTER
Institut für Angewandte Physik der Universität Kiel D-2300 Kiel 1, West Germany

(Received 7 March 1983)

Rotationally symmetric vortex flows between concentric cylinders with the inner one rotating and the outer one at rest have been investigated by numerical simulation and by laser-Doppler velocimetry for an annulus of aspect ratio $\Gamma = 1.05$ with a radius ratio $\eta = 0.5066$. Stationary states and relaxation towards them were explored close to the transition from the primary flow, which is mirror symmetric with respect to the midplane of the annulus, to a flow which gradually loses the symmetry. Detailed comparison of numerically simulated and measured velocity fields is made.

1. Introduction

The 'end effects' caused by rigid top and bottom plates on flows between concentric rotating cylinders have recently received increasing attention. Various theoretical and experimental investigations of their influence upon rounding of bifurcations, mode selection and stabilization, flow multiplicity, hysteresis, etc. have contributed to a discussion that was initiated by Benjamin (1978) and which at present does not seem to be settled (cf. Di Prima & Swinney 1981; Benjamin & Mullin 1982; and the papers cited therein).

Benjamin and Mullin have investigated flow changes in systems of small aspect ratios (annulus height/gap width) Γ over a wide range of Γ as a function of Reynolds number from a somewhat global point of view.‡ We study in this work in quantitative detail the rotationally symmetric flow in a short annulus of aspect ratio $\Gamma = 1.05$ with a radius ratio $\eta = 0.5066$. This system is strongly influenced by the rigid fixed top and bottom boundaries. They cause – independently of the size of Γ – the tangential velocity and centrifugal forces close to the rotating inner cylinder to drop off sharply towards the plates. The associated vertical pressure gradient generates axial flow close to the inner cylinder directed away from the plates into the annulus. This normally induces, i.e. after quasistatic increase of the Reynolds number, end rolls with inward flow near the plates (Pfister & Rehberg 1981).

Here the above mechanism generates a pair of vortex rolls well below the linear stability threshold R_c^∞ for onset of Taylor-vortex flow between infinitely long cylinders. Whereas there the rolls are nearly circular at R_c^∞ with diameter roughly

† Permanent address: Fachrichtung Theoretische Physik, Universität des Saarlandes, D-6600 Saarbrücken, West Germany.

‡ After submission of this paper we learned that Cliffe (1983) has numerically investigated the bifurcation structure of flows for small Γ.

given by the gap width d, here they are vertically compressed to about $\frac{1}{2}d$. With increasing Reynolds number this flow intensifies, retaining the mirror symmetry with respect to the midplane of the annulus up to a critical forcing R_c'. Then either the top or the bottom roll gradually grows with growing R at the expense of the other towards a flow state containing asymptotically at large R a single vortex cell of diameter d. For each value of the Reynolds number $R > R_c'$ there are two definite realizable flow configurations that are mirror images of each other.

Transitions between flows consisting of vortices with vertical extension $\gtrsim d$ and vortices compressed axially to about $\frac{1}{2}d$ have also been reported by Andreichikov (1977), Frank & Meyer-Spasche (1981) and Jones (1982) in annuli with periodic axial boundaries. However, in contradistinction to our rigid-end-dominated flow, the vortices in the above system had an axial size $\gtrsim d$ at smaller Reynolds numbers and were vertically compressed for larger driving. Also, solutions consisting of an alternating sequence of large and small vortices were found. While this feature resembles the flow in our system, it is obvious that the bifurcation behaviour of the periodically continued annulus is changed quite drastically into our experimentally observed bifurcation by imposing the experimental boundary conditions.

2. Methods of investigation

In this section we describe the system, the experimental set-up and the numerical simulation.

2.1. *The system*

We have investigated rotationally symmetric flows of an incompressible fluid in the annulus between two concentric cylinders. The inner one (radius r_1) was rotating with angular velocity Ω_1, and the outer cylinder (radius r_2) was at rest. The annulus length L determined by two stationary plates in contact with the fluid was nearly equal to the gap width $d = r_2 - r_1$ (cf. table 1). Hence the time for diffusion of momentum-density perturbations horizontally and vertically across the annulus is the same:

$$\tau = \frac{d^2}{2\pi\nu}. \tag{2.1}$$

Here ν denotes the kinematic viscosity of the fluid.

We will reduce the Reynolds number

$$R = \frac{\Omega_1 r_1 d}{\nu} \tag{2.2}$$

by the critical value R_c^∞ for onset of Taylor vortices between infinitely long cylinders (Kirchgässner 1961) with the same radius ratio $\eta = r_1/r_2$. It should be borne in mind that R_c^∞ is only a reference number without much meaning for our small system dominated by end effects.

2.2. *Experimental set-up*

In the experimental realization of the system described above silicone oil was used. Its viscosity (cf. table 1) was measured with an accuracy of 1 %. During the experiment the fluid was thermostated to within 0.05 K so that the corresponding drift of the considered Reynolds number did not exceed 0.1 %.

The gap between the cylinders of radii given in table 1 was uniform to within 0.1 % over the length $L_{\text{exp}} = (12 \pm 0.1)$ mm of the annulus. The deviation of the aspect ratio

$r_1 = 1.156$ cm	$r_2 = 2.282$ cm	$d = 1.126$ cm
$\eta = r_1/r_2 = 0.5066$	$\nu = 0.368$ cm^2/s	$R_c^\infty = 68.2$
$\tau = d^2/2\pi\nu = 0.548$ s	$L = 1.1823$ cm	$\Gamma = L/d = 1.05$

TABLE 1

$\Gamma_{\text{exp}} = 1.066 \pm 0.009$ from the value $\Gamma = 1.05$ used in the numerical simulation is too small to be resolved in our figures. Since we do not expect it to be relevant, we shall ignore it in the following. The angular velocity of the inner cylinder was electrically controlled with an accuracy of 0.5 % for short-time averages, e.g. over one rotation, and of 0.05 % for long-time averages.

The local radial velocity was measured by a real-fringe Doppler anemometer using a tracker for analog recording of the velocity. Details of the velocity measurement method are explained in Vehrenkamp *et al.* (1979). The measurement volume of rough size $0.1 \times 0.1 \times 0.5$ mm^3 was positioned by a motor-driven lift and an (x, y)-table. We estimated the inaccuracy of the radial velocity measurement to be less than about 1.0 cm/s, i.e. less than 2–3 times the size of the dots used in our figures below. This error comes almost entirely from inaccuracies in the localization of the scattering volume. Thereby the other velocity components contribute to the scattered light signal.

2.3. *Basic equations*

Our theoretical investigation starts from the standard Navier–Stokes equations for the velocity field $\boldsymbol{u}(\boldsymbol{r}, t)$ written with the help of the incompressibility condition

$$D = \nabla \cdot \boldsymbol{u} = 0 \tag{2.3}$$

in the form

$$\partial_t u_\alpha + \nabla_\beta (u_\beta u_\alpha) = -\nabla_\alpha P - \nu [\nabla \times (\nabla \times \boldsymbol{u})]_\alpha, \tag{2.4}$$

which we found most convenient to solve numerically (for a discussion see Welch *et al.* 1966). The numerical simulation of the flow is based upon the above time-dependent equations. We were not only interested in stationary final flow states but also in the time evolution towards them. For example, we determined how the flow evolved, either starting from different initial states or as a function of different histories $R(t)$ of the Reynolds number or in response to some imposed perturbation.

In (2.4) $P(\boldsymbol{r}, t) = p(\boldsymbol{r}, t)/\rho$ denotes the dynamic pressure divided by the mass density ρ. Its relation to the velocity field is given by the Poisson equation

$$\nabla^2 P = -\nabla_\alpha \nabla_\beta (u_\alpha u_\beta) - \partial_t D, \tag{2.5}$$

which connects the longitudinal parts of (2.4). Here we have deliberately kept the term $\partial_t D = \partial_t \nabla \cdot \boldsymbol{u}$, which vanishes according to (2.3). Solving the above equations approximately on a lattice in space and time one should retain the discretized version of $\partial_t D$ even though the appropriate restrictions aiming at $D = 0$ are enforced (Welch *et al.* 1966).

For the rotationally invariant flows considered in this work, (2.4), (2.5) in a cylindrical coordinate system become

$$\partial_t u + \frac{1}{r}\partial_r (ru^2) - \frac{v^2}{r} + \partial_z (uw) = -\partial_r P - \nu \partial_z (\partial_r w - \partial_z u), \tag{2.6a}$$

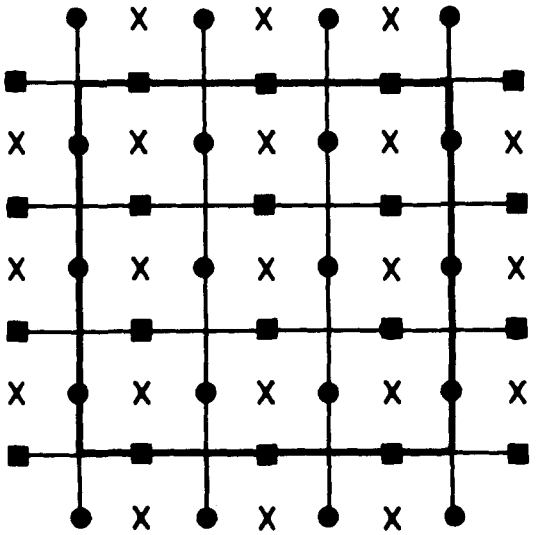

FIGURE 1. Structure of the discretization lattices in the (r, z)-plane of the annulus for the radial velocity u (●), the axial velocity w (■), the tangential velocity v and the pressure P (×). Thick full lines denote the boundaries of the annulus at r_1, r_2 (vertical lines) and at $z = \pm\frac{1}{2}L$ (horizontal lines).

$$\partial_t v + \frac{1}{r}\partial_r(ruv) + \frac{uv}{r} + \partial_z(vw) = \nu\partial_z^2 v + \nu\partial_r\left(\frac{1}{r}\partial_r(rv)\right), \tag{2.6b}$$

$$\partial_t w + \frac{1}{r}\partial_r(ruw) + \partial_z w^2 = -\partial_z P + \frac{\nu}{r}\partial_r(r\partial_r w - r\partial_z u), \tag{2.6c}$$

$$\partial_z^2 P + \frac{1}{r}\partial_r(r\partial_r P) = -\frac{1}{r}\partial_r^2(ru^2) - \partial_z^2 w^2 - 2\partial_r\partial_z(uw) + \frac{1}{r}\partial_r v^2 - \frac{2}{r}\partial_z(uw) - \partial_t D, \tag{2.6d}$$

with

$$D = \frac{1}{r}\partial_r(ru) + \partial_z w. \tag{2.7}$$

Here the radial velocity u, the tangential or azimuthal velocity v, the axial velocity w and the pressure depend on r, z and t.

2.4. *Numerical simulation*

We have solved (2.6) with the appropriate boundary conditions on a lattice (see below) with an explicit finite-difference method using forward differences for ∂_t and central differences for spatial derivatives, with a truncation error $O(\Delta t, \Delta x^2)$. The procedure is as follows. Given the velocity field at time t_n, we determine the pressure $P(t_n)$ by solving the discretized version of the Poisson equation (2.6*d*) iteratively by successive over-relaxation. This is the most time-consuming part of the program. To optimize it we extrapolate with orthogonal polynomials the previously determined pressures $P(t_m < t_n)$ in order to obtain good start values for the iteration. That can reduce the number of iterations by roughly a factor of three in comparison with unextrapolated start values $P(t_{n-1})$. The rate of change of D entering (2.6*d*) is approximated by $-D(t_n)/\Delta t$, thus imposing the incompressibility restriction via

$D(t_{n+1}) = 0$. Having determined $P(t_n)$, we obtain the velocity field at time t_{n+1} by a forward time step of (2.6*a–c*).

Our lattice in the (r, z)-plane consists of three interlacing sublattices as shown schematically in figure 1: one (●) for the radial velocity u, one (■) for the axial velocity w, and one (×) for the tangential velocity v and the pressure P. This lattice structure enforces correct momentum balance of the discretized equations (2.6*a–c*) for every cell indicated by thin lines in figure 1 (cf. Welch *et al.* 1966; Mihelcic *et al.* 1981).

The position of the lattice points and their spacings are chosen such that the fluid boundaries (full lines in figure 1) lie halfway between pressure points × . So the top and bottom boundaries of the annulus go through w-points ■. The vertical boundaries at r_1, r_2 go through u-points ●. Note that there is one layer of lattice points outside the annulus, as indicated in figure 1. In this work we impose rigid (no-slip) boundary conditions everywhere. They are implemented in two different ways; (i) at those points lying on a boundary we fix the corresponding velocity component to have the appropriate value, e.g. $u(\bullet) = 0$ at $r = r_1, r_2$; (ii) for those components for which the lattice points do not fall on a boundary we enforce the average over the two points on either side of the boundary to have the appropriate value, e.g. $w(\blacksquare)_{\text{inside}} + w(\blacksquare)_{\text{outside}} = 0$ at $r = r_1, r_2$ or $\frac{1}{2}(v(\times)_{\text{outside}} + v(\times)_{\text{inside}}) = \Omega_1 r_1$ at r_1. Theoretical problems arise with the non-discretized Navier–Stokes equations in the corners near the inner cylinder from the discontinuity of the boundary condition for the tangential velocity. Experimentally, however, our LDV measurements, which could be done down to distances of about 0.2 mm from the inner corners, showed no anomalies there but a perfectly smooth velocity field. So if corner anomalies exist (which seems doubtful in view of the small gap separating the inner cylinder from the rigid fixed end) they are localized on a scale smaller than 0.2 mm. For this and other reasons, we therefore chose an arrangement of the v-points that circumvents the theoretical problem, as shown in figure 1. With our closest v-points still being 0.4 mm (0.2 mm for control runs with the finer mesh described below) away from the corners there were no numerical problems. The tangential velocity interpolated linearly along the horizontal and vertical 'lattice bonds' that connect the inner × close to the corner to the two outer × varies smoothly from $\Omega_1 r_1$ at r_1 to zero at the rigid end plate. Evidence for the fact that our simulation is accurate enough to yield the velocity field in the annulus on scales of our discretization may be derived from the comparison with experiments in §3.

Results reported here were obtained on uniform lattices with a spacing between like points of

$$\frac{\Delta r}{d} = \frac{\Delta z}{d} = 0.05$$

using a time step of

$$\frac{\Delta t}{\tau} = 2.74 \times 10^{-3}.$$

For the above discretization the CPU time for a simulation of the flow for a time τ was about 29.7 s on an IBM 3033. To check the numerical accuracy we ran a few simulations on a lattice with half the above spacing and a time step reduced by about a factor four. The velocity differences nowhere exceeded 0.4 cm/s, i.e. four times the line width used in our figures for the velocity field. Mostly they were much smaller.

3. Results

The main result of our investigation is the elucidation of a second-order transition from a flow consisting of one compressed Taylor vortex pair, which is mirror-symmetric with respect to the midplane of the annulus, to a flow that (gradually) loses this symmetry upon increasing the Reynolds number beyond a critical $R_c' \approx 1.88 R_c^\infty$. At this supercritical bifurcation one of the vortex rolls starts growing at the expense of the other towards a flow consisting asymptotically of a single vortex roll in the annulus. Furthermore, the results demonstrate that our numerical simulation of the flow and the measured velocity field agree quantitatively.

3.1. *The velocity field*

The velocity field in our small system is strongly influenced by the rigid top and bottom plates. They cause the tangential velocity to drop to zero and thereby induce radial flow for all Reynolds numbers as described in §1. These strong boundary 'perturbations' prevent the detection of remnants of the bifurcation in the 'ideal' ($\Gamma = \infty$) system from circular Couette flow to Taylor-vortex flow at R_c^∞. In the $\Gamma = 1.05$ annulus the flow consists, even well below R_c^∞, of two compressed Taylor vortices with radial velocities that increase smoothly with R. Figure 2(*a*) shows a vertical cross-section of the rolls at $R/R_c^\infty = 1.30$, i.e. $\epsilon' = -0.31$, where

$$\epsilon' = (R - R_c')/R_c'. \tag{3.1}$$

The photo of the laser-illuminated (r, z)-plane of the fluid was made through a cylindrical lens. The arrows denoting the calculated velocity field projected onto the (r, z)-plane demonstrate the overall agreement of numerically simulated and experimental flow pattern.

As an aside we mention that we observed for the Reynolds number of figure 2(*a*) a small counter-circulating Moffat eddy (Moffat 1964; Moore 1981) in the top and bottom right-hand corners only with our finer mesh. The largest amplitude of this recirculating flow is only about 1.5×10^{-4} of the largest radial flow in the midplane of the annulus. Since this effect is too fine to be detected in our laser-Doppler measurements as well as in the simulation with the coarse grid, it will not be discussed further.

The flow remains mirror-symmetric with respect to the midplane of the annulus at $z = 0$,

$$u(z) = u(-z), \quad v(z) = v(-z), \quad w(z) = -w(-z), \tag{3.2}$$

up to $R_c' \approx 1.88 R_c^\infty$. That seems to corroborate an estimation of the onset of asymmetry at $R_c' \approx 2.0 R_c^\infty$ obtained (Benjamin & Mullin 1981) from flow observations in a system with the same aspect ratio but with a larger ratio $\eta = 0.615$ of radii.

On increasing R beyond R_c', the flow becomes gradually asymmetric (for a more detailed discussion see below). One roll – in figures 2 and 3 the upper one – grows and the other one decreases. Thereby the centre of the growing roll moves towards the centre of the annulus, while the smaller one is pushed into the lower left corner. At large R, e.g. $R = 2.61 R_c^\infty$, i.e. $\epsilon' = 0.39$ shown in figure 2(*b*), the big roll fills almost the whole annulus, but a small one is still present close to the inner cylinder. The latter reflects the inward radial and axial flow that is induced by the sharp drop of the tangential velocity close to the inner cylinder towards the rigid fixed plate. The associated vertical pressure gradient favouring inwards-directed axial flow close to the inner cylinder lets the small roll survive against the tendency to form circular rolls. Note the agreement of flow simulation and experiment on this subtle feature.

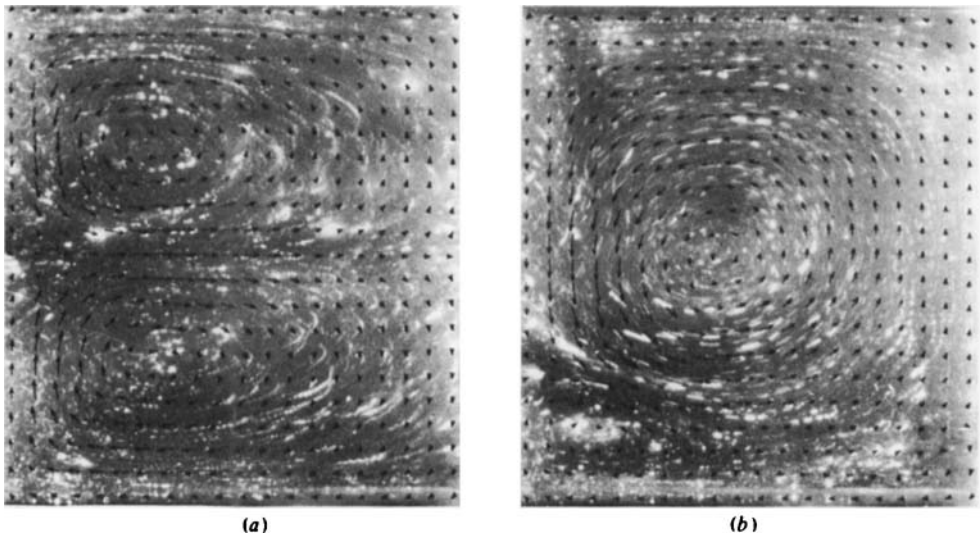

FIGURE 2. Photographs of the vortex flow in a vertical cross-section of the annulus: (*a*) below threshold for onset of asymmetric flow, $\epsilon' = -0.31$; (*b*) above threshold, $\epsilon' = 0.3$. The left (right) boundary is the inner (outer) cylinder. Arrows denote the simulated velocity field.

Figure 3 shows the stationary velocity field in the middle of the gap at $r = r_1 + \frac{1}{2}d$ as a function of z for various ϵ' between -0.31 and $+0.38$. For $\epsilon' < 0$ the above graphs have the mirror symmetry (3.1): at $z = 0$ the flow is outwards, $u > 0$, and near the top and bottom plates it is inwards, $u < 0$. With increasing $\epsilon' > 0$ the maximum of the radial (and tangential) velocity, i.e. the position of largest outward flow, as well as the zeros of u marking the border between inward and outward flow move downwards in the annulus.

The measured radial velocity (dots) shows close to the transition $\epsilon' = 0$ a larger asymmetry than the numerically simulated u (full line). This difference is presumably due to boundary imperfections of the experimental setup. The latter induce symmetry-breaking flow already below threshold (cf. figure 3*b*). In addition, they enhance the asymmetry above (cf. figures 3*c*, *d*), thus causing appreciable experimental rounding of the bifurcation at $\epsilon' = 0$. For larger distances $|\epsilon'|$ from threshold, however, the experimental imperfections are less influential. Therefore the differences in figures 3 (*a*, *e*) between simulated and experimental velocity fields become smaller and lie within the combined error bounds of both approaches. In view of these circumstances we consider the agreement between simulation and experiment to be good. That holds true also for the radial velocity field measured at the distance $\frac{1}{4}d$ from the inner cylinder as a function of z.

3.2. *The bifurcation*

To describe the above bifurcation more quantitatively we introduce the parameter

$$P = \frac{\int \mathrm{d}r\,\mathrm{d}z\,(u(r,z) - u(r,-z))}{\int \mathrm{d}r\,\mathrm{d}z\,(|u(r,z)| + |u(r,-z)|)}, \tag{3.3}$$

which measures the deviation of the radial velocity field from the mirror symmetry. The integrations in (3.3) extend over a vertical cross-section of the annulus. P

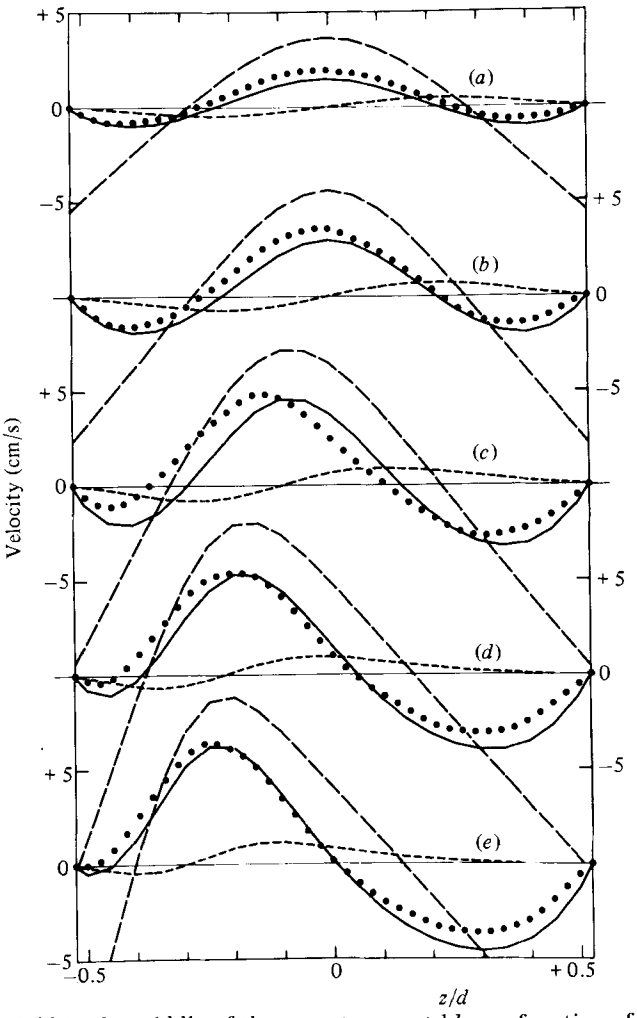

FIGURE 3. Velocity field in the middle of the gap at $r = r_1 + \frac{1}{2}d$ as a function of height z/d for five different $\epsilon' = (R - R_c')/R_c'$: (*a*) −0.31; (*b*) −0.13; (*c*) 0.039; (*d*) 0.21; (*e*) 0.38. Dots represent the measured radial velocity. Piecewise linear curves connect the numerically obtained velocities: ——, u; – – –, $v - \langle v \rangle$; ·····, w. The average $\langle v \rangle$ of v in the middle of the gap along z can be read off at $z/d = \pm\frac{1}{2}\Gamma$, where $v = 0$.

vanishes in the symmetric phase. Furthermore, it is normalized such that $|P| = 1$ for a single vortex roll with $u(z) = -u(-z)$. The signature of P discriminates the position of the growing vortex: for positive (negative) P the bottom (top) roll is the larger one. Here, as throughout this paper, u is defined to be positive for outward flow. The asymptotic value $P = +1$ ($P = -1$) denotes a single clockwise (counter-clockwise) swirling vortex that has grown out of the bottom (top) vortex.

The Navier–Stokes equations (2.6) with mirror-symmetric boundaries are invariant under the mirror operation

$$u(z) \to u(-z), \quad v(z) \to v(-z), \quad w(z) \to -w(-z). \tag{3.4}$$

Therefore two flows that are transformed into each other by the operation (3.4) are equivalent and have the same value of $|P|$. Hence the bifurcation diagram of P versus

Reynolds number is symmetric in the absence of imperfections breaking the mirror symmetry.

Of course there are always such imperfections present not only in the experiment but also in the numerical simulation. Our experimental imperfections selected the $P < 0$ states with the larger roll on top when R was increased gradually, while $P > 0$ states could be prepared by sudden starts of the inner cylinder to a high Reynolds number with a subsequent gradual decrease. In the numerical simulation, on the other hand, we generated $P > 0$ states by increasing the Reynolds number gradually or in several smaller steps to $R > R_c'$. To obtain $P < 0$ states numerically we first increased R from zero to a value well above R_c', e.g. $\epsilon' = 0.38$. After the resulting flow with the large roll on top had become stationary, we varied ϵ' to the desired final value either gradually, or in several steps, or in one step, thereby producing in each case the same flow.

With these two different procedures we could numerically generate for any given $R > R_c'$ two different stationary, stable flow fields which – within our numerical accuracy – could be transformed into each other by the mirror operation (3.4) and which thus had the same value of $|P|$. We therefore conclude that symmetry-breaking imperfections inherent in the numerical simulation are too small to cause an appreciable rounding of the bifurcation by enhancing the asymmetry of a particular flow realization. But they are sufficiently large to bias the evolution from an initial symmetric state towards a final asymmetric flow in response to different histories $R(t)$ of the driving.

Figure 4 shows the numerically obtained bifurcation diagram. Since we found the transition to be symmetric the absolute value of P is plotted versus Reynolds numbers. The dots denote stationary flows. Triangles ▲(▼) represent transient states which were realized upon increasing (decreasing) the Reynolds number continuously along a ramp between $\epsilon' \approx -0.3$ and $\epsilon' \gtrsim 0.5$ with a ramp rate of $|\mathrm{d}\epsilon'/\mathrm{d}t| = 1.055 \times 10^{-2}/\tau$. Note the hysteresis of P for the non-stationary flows.

We extend our simulation up to $R = 4.4R_c^\infty$, for which value $|P| = 0.95$ was still below its asymptotic limit. The small countercirculating vortex causing this deviation of $|P|$ from 1 could be seen in the experimental flow realization in a corner near the inner cylinder for even larger Reynolds numbers up to the onset of time-dependent flow.

3.3. *Critical slowing down*

We fitted the first few dots of figure 4 above the transition to a square root and thus obtained $R_c' \approx 1.88R_c^\infty$ and $P \approx \pm 2.45(\epsilon')^{\frac{1}{2}}$ close to the threshold. To check the above value of R_c' we determine the critical slowing down of the relaxation rates $\gamma(R_i \to R_f)$ for final Reynolds numbers close to the transition. Here $\gamma(R_i \to R_f)$ is the inverse of the time the system needs to relax to the stable stationary flow at R_f after an instantaneous step of R from R_i of R_f. Our definition of that time required velocities of appreciable size to be stationary with respect to the first four significant digits. These results gave also $R_c' \approx 1.88R_c$ as the (final) Reynolds number for which γ diverges. Close to R_c', i.e. for $|\epsilon_f'| \lesssim 0.15$, γ was practically independent of R_i: the relaxation rates after steps from various initial states to various final states $\epsilon' \gtrless 0$ close to the transition could be parametrized well by

$$\gamma \approx \frac{0.77}{\tau}\epsilon'. \tag{3.5}$$

Here γ is defined to be negative for final states $\epsilon' < 0$.

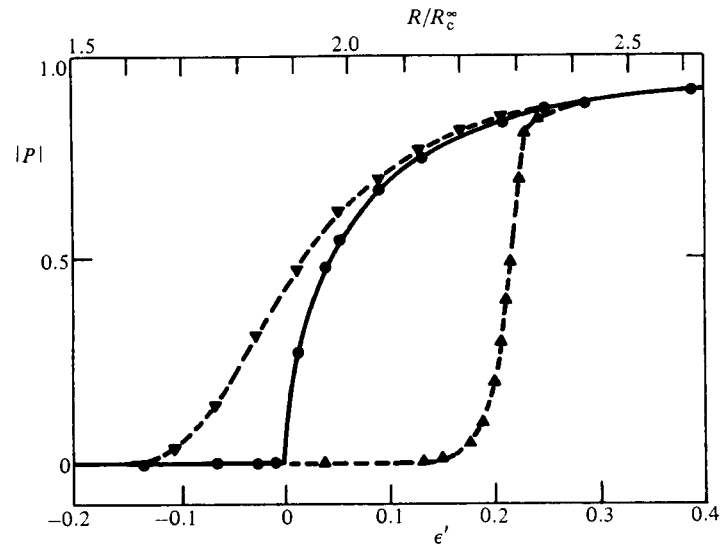

FIGURE 4. Numerically obtained bifurcation of the parameter P (3.3) measuring the radial velocity field's deviation from mirror symmetry. Dots denote stationary flows. The triangles represent transient states which were realized by increasing (▲) or decreasing (▼) the Reynolds-number along a ramp with a rate $|d\epsilon'/dt| = 1.055 \times 10^{-2}/\tau$. Lines are guides to the eye. The full curve close to the bifurcation is the fit $|P| = 2.45(\epsilon')^{\frac{1}{2}}$ obtained from the first few dots above threshold. See text for details concerning the symmetry of the bifurcation.

We also evaluated torques and the volume-averaged dissipation to see whether they showed any sign of the transition. Within our resolution the answer was no. The torque on the inner (outer) cylinder normalized by the torque for ideal Couette flow between infinitely long cylinders increased very smoothly in the range $-0.3 \leqslant \epsilon' \leqslant 0.4$ from 2.62 to 2.95 (0.36–0.57). The volume-averaged dissipation reduced by that of ideal Couette flow also increased smoothly – from 2.43 to 2.72 – without showing any hint of a transition.

4. Summary

We have investigated rotationally symmetric vortex flows in an annulus of aspect ratio $\Gamma = 1.05$ by numerical simulation and by laser-Doppler velocimetry with the following results: up to a threshold at $R_c' \approx 1.88 R_c^\infty$, the flow is mirror-symmetric across the midplane of the annulus consisting of two vertically compressed vortex rolls. They are present well below the theoretical critical Reynolds number R_c^∞ for onset of Taylor-vortex flow in the infinitely extended annulus.

Above threshold the flow gradually becomes asymmetric. On increasing $\epsilon' = (R - R_c')/R_c'$, either the top or the bottom roll grows, while the other one shrinks and is pushed into a corner near the inner cylinder. At large ϵ' the flow contains asymptotically a single vortex of diameter $\approx d$, although a small remnant of the second vortex survives in the corner for reasons already explained.

For any particular $\epsilon' > 0$ two definite flows being mirror images of each other are possible. A properly defined parameter $P(\epsilon')$ measurng the global deviation from mirror symmetry shows a symmetric supercritical bifurcation. Close to the threshold $\epsilon' = 0$ we found $P \approx \pm 2.45(\epsilon')^{\frac{1}{2}}$ for stationary states where the two branches denote the two flows described above. Transient non-stationary states prepared by varying

ϵ' through threshold along a ramp show hysteresis. The position of the threshold was checked by investigating the critical slowing down of the flow. The time the system needs to relax towards the final stationary flow at ϵ'_f after a sudden variation from an initial value ϵ'_i is practically independent of ϵ'_i near the threshold $\epsilon'_f = 0$ and increasesd there $\sim 1/|\epsilon'_f|$.

The experimental set-up had sufficiently large symmetry-breaking boundary imperfections to induce asymmetric flow below threshold, to enhance the flow with the large roll on top ($P < 0$), and thus to cause rounding of the favoured bifurcation branch. States with $P > 0$ were obtained experimentally by sudden starts of the inner cylinder. Also the numerical simulation has inherent 'imperfections'. Although they are too small to cause numerically relevant asymmetry in the bifurcation diagram $P(\epsilon')$, they are large enough to bias the time evolution of flows in response to different histories of the forcing: increasing the Reynolds number smoothly through $\epsilon' = 0$ generates $P > 0$ states (small roll on top). The corresponding mirror image (large roll on top) can be produced in the simulation by a procedure completely analogous to the experimental one: (i) sudden start of the inner cylinder to a value of ϵ' well above threshold; (ii) relaxation; (iii) gradual decrease of ϵ' to the desired value $\epsilon' > 0$.

Taking experimental imperfections into account, the agreement between measured and simulated radial velocity fields is good. This seems to be the first numerical simulation of velocity fields in the Taylor system that agree quantitatively with measured ones.

One of us, G.P., acknowledges support of the Stiftung Volkswagenwerk.

REFERENCES

ANDREICHIKOV, I. P. 1977 *Isv. Akad. Nauk SSSR, Mekh. Zhid. i Gaza* **12**, 47 [English transl. *Fluid Dyn.* Sept. 1977, p. 38].

BENJAMIN, T. B. 1978 *Proc. R. Soc. Lond.* A **359**, 1, 27.

BENJAMIN, T. B. & MULLIN, T. 1981 *Proc. R. Soc. Lond.* A **377**, 221.

BENJAMIN, T. B. & MULLIN, T. 1982 *J. Fluid Mech.* **121**, 219.

CLIFFE, K. A. 1983 *J. Fluid Mech.* **135**, 219.

DI PRIMA, R. C. & SWINNEY, H. L. 1981 In *Hydrodynamic Instabilities and the Transition to Turbulence* (ed. H. L. Swinney & J. P. Gollub), pp. 139–180. Springer.

FRANK, G. & MEYER-SPASCHE, R. 1981 *Z. angew. Math. Phys.* **32**, 710.

JONES, C. A. 1982 *J. Fluid Mech.* **120**, 433.

KIRCHGÄSSNER, K. 1961 *Z. angew. Math. Phys.* **12**, 14.

MIHELCIC, M., SCHRÖCK-PAULI, C., WINGERATH, K., WENZL, H., UELHOFF, W. & VAN DER HART, A. 1981 *J. Crystal Growth* **53**, 337.

MIHELCIC, M., SCHRÖCK-PAULI, C., WINGERATH, K., WENZL, H., UELHOFF, W. & VAN DER HART, A. 1982 *J. Crystal Growth* **57**, 300.

MOFFAT, H. K. 1964 *J. Fluid Mech.* **18**, 1.

MOORE, D. R. 1981 Contribution to the second Taylor Vortex Working Party at Tufts University, USA.

PFISTER, G. & REHBERG, I. 1981 *Phys. Lett.* **83A**, 19.

VEHRENKAMP, R., SCHÄTZEL, K., PFISTER, G., FEDDERS, B. S. & SCHULZ-DUBOIS, E. O. 1979 *Phys. Scr.* **19**, 379.

WELCH, J. E., HARLOW, F. H., SHANNON, J. P. & DALY, B. J. 1966 *Los Alamos Sci. Lab. Rep.* LA-3425.